Three-Dimensional Distribution of Cardiac Na^+-Ca^{2+} Exchanger and Ryanodine Receptor during Development

Pauline Dan,*† Eric Lin,*† Jingbo Huang,*† Perveen Biln,*† and Glen F. Tibbits*†

*Cardiac Membrane Research Laboratory, Simon Fraser University, Burnaby, British Columbia, Canada; and †Cardiovascular Sciences, Child and Family Research Institute, Vancouver, British Columbia, Canada

ABSTRACT Mechanisms of cardiac excitation-contraction coupling in neonates are still not clearly defined. Previous work in neonates shows reverse-mode Na^+-Ca^{2+} exchange to be the primary route of Ca^{2+} entry during systole and the neonatal sarcoplasmic reticulum to have similar capability as that of adult in storing and releasing Ca^{2+}. We investigated Na^+-Ca^{2+} exchanger (NCX) and ryanodine receptor (RyR) distribution in developing ventricular myocytes using immunofluorescence, confocal microscopy, and digital image analysis. In neonates, both NCX and RyR clusters on the surface of the cell displayed a short longitudinal periodicity of $\sim$0.7 μm. However, by adulthood, both proteins were also found in the interior. In the adult, clusters of NCX on the surface of the cell retained the $\sim$0.7-μm periodicity whereas clusters of RyR adopted a longer longitudinal periodicity of $\sim$2.0 μm. This suggests that neonatal myocytes also have a peri-M-line RyR distribution that is absent in adult myocytes. NCX and RyR colocalized voxel density was maximal in neonates and declined significantly with ontogeny. We conclude in newborns, Ca^{2+} influx via NCX could potentially activate the dense network of peripheral Ca^{2+} stores via peripheral couplings, evoking Ca^{2+}-induced Ca^{2+} release.

INTRODUCTION

In adult mammalian ventricular myocytes, excitation-contraction (E-C) coupling occurs primarily through Ca^{2+}-induced Ca^{2+} release (CICR) (1), which is initiated by membrane depolarization, causing a Ca^{2+} influx via the opening of dihydropyridine receptors ((DHPR) or L-type Ca^{2+} channels). This influx in turn acts as a trigger to activate a greater and graded release of Ca^{2+} from the sarcoplasmic reticulum (SR) via the ryanodine receptors (RyR), resulting in a rapid rise in free cytosolic Ca^{2+} concentration and contraction.

The functional coupling of DHPR and RyR hinges upon a close spatial relationship. At the dyad, DHPR in the T-tubular membrane and RyR in the junctional SR membrane are directly apposed, separated only by a diffusion-limited space of $<$20 nm (2). Their juxtaposition ensures that when DHPR open, RyR in the immediate vicinity sense a substantially large and rapid rise in free local Ca^{2+} concentration, critical to RyR activation (3). This organization permits SR Ca^{2+} release at each junction to be tightly regulated by only local DHPR, underpinning the local control theory of cardiac E-C coupling.

Mechanisms of E-C coupling in neonatal hearts are still not clearly defined. At early stages, the myocardium undergoes rapid growth, accompanied by morphological changes that markedly impact contractile function; T-tubules are either absent or poorly developed. Neonatal myocytes appear to have a different mechanism of E-C coupling than that in the adult. Unlike adults, Ca^{2+} influx via DHPR and DHPR-mediated CICR contributes little to E-C coupling. DHPR blockers have negligible effects on both Ca^{2+} transients (4) and muscle contractions (5) in newborn ventricular myocytes. However, DHPR blockers applied to adult cells result in cessation of Ca^{2+} transients.

Investigations into the role of SR Ca^{2+} release on neonatal E-C coupling have yielded conflicting results. Some indicate SR blockers to decrease neither the activator Ca^{2+} transient nor the contractile force in newborn ventricles (6–8), while others demonstrate these responses to be significantly diminished upon SR blockade (9,10). Recent work shows the neonatal ventricular SR to have at least the same capability as that of adults in both storing and releasing Ca^{2+} (4,6,11) when normalized per unit cell volume. Furthermore, RyR from both newborn and mature cardiomyocytes exhibit similar gating, permeation, and ligand binding properties (6) in planar lipid bilayers.

In studies of neonatal E-C coupling, there is a general consensus that reverse-mode Na^+-Ca^{2+} exchange (NCX) is the main route of entry for activator Ca^{2+} during systole (5, 12,13). Depolarization-induced Ca^{2+} influx via NCX could directly elicit contractions in neonatal ventricular myocytes (5,12). Consistent with this observation NCX mRNA, protein expression, and current density are maximal near birth, being 2.5- to 6-fold greater than those observed in mature cells, and decline postnatally to adult levels by $\sim$3 weeks of age (13–15).

We recently reported a novel finding in the mechanism of newborn cardiac E-C coupling. Using electrophysiological and Ca^{2+} imaging techniques, we demonstrated in neonatal

Submitted January 21, 2007, and accepted for publication May 29, 2007.

Pauline Dan and Eric Lin contributed equally to this work.

Address reprint requests to Glen F. Tibbits, PhD, Cardiac Membrane Research Laboratory, Kinesiology, Simon Fraser University, Burnaby, BC, Canada V5A 1S6. Tel.: 604-291-3658; Fax: 604-291-3040; E-mail: tibbits@sfu.ca.

Editor: David A. Eisner.

0006-3495/07/10/2504/15 $2.00

doi: 10.1529/biophysj.107.104943

rabbit ventricular myocytes that reverse-mode NCX was functionally coupled to RyR to initiate CICR, the efficacy of which attenuated with development (16). We hypothesized, therefore, that NCX colocalizes with RyR in the neonatal heart and that this colocalization declines with ontogeny. To test this, we used immunofluorescence, confocal microscopy, deconvolution, and digital image analysis to measure the regional distribution and colocalization of NCX and RyR in developing rabbit ventricular myocytes.

MATERIALS AND METHODS

All chemicals used were obtained from Sigma (St. Louis, MO) unless otherwise stated. Animal handling was done in compliance with the guidelines of the Canadian Council on Animal Care.

Cell isolation and preparation

Ventricular myocytes were isolated from the hearts of New Zealand White rabbits (of either sex) from five age groups (3 (3d; $N = 15$ cells), 6 (6d; $N = 10$ cells), 10 (10d; $N = 25$ cells), 20 (20d; $N = 22$ cells), and 56 (56d; $N = 14$ cells) days postpartum; four animals per group) using an age-specific collagenase-based digestion technique described previously (4). Freshly isolated myocytes were fixed in 2% paraformaldehyde (10 min), quenched by 100 mM glycine (10 min), permeabilized with 0.1% Triton X-100 (10 min), and washed 3×10 min in phosphate buffered saline. Fixed cells were adhered to poly-L-lysine coated coverslips and subsequently labeled.

Immunocytochemistry

Fixed cells were incubated with primary antibodies raised against the cardiac NCX1 (0.23 μg/ml; mouse anti-NCX1 (C2C12); IgM; Affinity Bioreagent, Golden, CO) and RyR2 (5 μg/ml; mouse anti-RyR2 (C3-33); IgG_1; Affinity Bioreagent) overnight at 4°C. The specificity of both antibodies in cardiac ventricular myocytes has been extensively described (7,17–20). After incubation, cells were washed for 3×10 min, and incubated in fluorophore-conjugated, secondary antibodies (4 μg/ml; Alexa Fluor 488 goat anti-mouse IgG_1 and Alexa Fluor 555 goat anti-mouse IgM) for 1 h at room temperature. Then cells were washed for 3×10 min and mounted onto coverslips with Molecular Probes Slow Fade Gold anti-fade reagent (Invitrogen Canada, Burlington, ON). Coverslips were fixed onto the slide with nail polish.

Two sets of control experiments were performed. First, cells were labeled with an irrelevant, isotype-specific (IgG_1 or IgM), primary antibody and its corresponding secondary antibody. Second, cells that had been labeled with the primary monoclonal IgM directed against NCX were incubated with an anti-mouse IgG_1 secondary antibody; cells that had been labeled with the primary monoclonal IgG_1 directed against RyR were incubated with an anti-mouse IgM secondary antibody. Images of these control experiments showed only dim, diffuse, nonspecific staining.

Image acquisition and deconvolution

Images of labeled cells were acquired with a Zeiss (Jena, Germany) LSM 5 Pascal laser scanning confocal microscope equipped with a Zeiss 63×/1.4 Plan-Apochromat oil immersion objective. The acquisition software was LSM5 Pascal version 2.8 SP1. The 543 and 488 nm excitation beams were supplied by helium-neon and argon lasers (Zeiss LSM5 Pascal laser module), respectively. A series of two-dimensional images were acquired through the depth of the cell, using a voxel dimension of $100 \times 100 \times 200$ nm (axial). A typical image stack contained 40–80 images. Emission was captured sequentially to minimize signal bleed-through and the confocal pinhole was set at one Airy disk.

To increase the resolution of the data, images were deconvolved using a maximum likelihood estimation algorithm (Huygens Pro 2.4.1 Linux-based software; Scientific Volume Imaging, Hilversum, The Netherlands). The point spread function for deconvolution was determined empirically using 100-nm diameter fluorescent beads (Invitrogen Canada; (21)). Representative images are shown in Figs. 1–4.

The fullwidth at half-maximum intensity (FWHM) of a deconvolved image of a fluorescent bead labeled with Texas Red was 250 nm in both *x*- and *y*-dimensions. In the *z*-direction, the FWHM was 620 nm. Comparable FWHM values were obtained for fluorescein beads. Therefore, the voxel dimensions used for this study satisfied the Nyquist criterion for sampling.

Image analysis

Colocalization in whole cell

To measure NCX and RyR colocalization in the whole cell, deconvolved images were processed using Imaris 4.0 (Bitplane, Saint Paul, MN) software. Images of control cells, dual labeled with irrelevant primary antibodies and appropriate secondary antibodies were used to determine a threshold value that eliminated >99% of the voxels in these control images (18,22,23). This threshold was applied to images of fully labeled cells; voxels with intensities lower than the threshold were set to zero, whereas voxels containing intensities greater than the threshold remained unaltered. After thresholding, only those voxels with identical *x*-, *y*-, and *z*-coordinates were considered to be colocalized.

Cell layering

Details of this procedure are documented in the Supplementary Material. In brief, a myocyte outline was created using the corresponding stacks of binary images of NCX and RyR label. The two stacks of binary images were combined and morphological closing was applied to each optical plane (*xy*) to extrapolate the cell boundary. The closed optical planes were merged to form a binary three-dimensional (3-D) cell outline and segmented into layers across its diameter, as illustrated (see Fig. 5 *A*). The outermost layer, the cell boundary, was designated as layer 1. Each successive inward layer was one voxel thick (layers not drawn to scale) and numbered in ascending order. An additional layer, denoted layer 0, was included just outside the surface to account for the uncertainty in identifying the cell boundary. The volume (in picoliter (pL)) of each cell layer was determined by calculating the number of voxels contained within that layer.

After layering, the fully labeled cell was thresholded according to values obtained from control images. The proportion of NCX or RyR voxels contained within each cell layer was determined by ''the number of labeled voxels within a given layer'' divided by ''the number of labeled voxels in all layers'' of the cell.

Intercluster distance analysis

Details of this procedure are documented in the Supplementary Material. In brief, the intercluster spacing of peripheral NCX or RyR clusters was determined by measuring the longitudinal distance between fluorescent clusters at the boundary of the myocyte. The analysis was performed on 18–35 central optical planes, depending on cell size, of each cell. Within each plane, the full length of each of the two cell edges was analyzed to avoid biases. As shown in Fig. 5 *B*, the cell edge was delineated by a 3-pixel-thick band (*red*; not drawn to scale), defined by eroding the optical planes (*xy*) of the previously determined cell outline. Each cluster of label was reduced to a single point by calculating the center-of-fluorescence. Point-to-point separation distance was measured by initially identifying two points that were the farthest from each other, and then connecting all points in between by identifying the next nearest point, beginning from an end point. The probability of observing a

particular intercluster spacing in each cell was calculated by ''the frequency of observing a particular intercluster distance'' divided by ''the total number of intercluster distances recorded'' in that cell.

Measurements of NCX-labeled vesicular structures or longitudinal periodicity of transverse rows of NCX or RyR labeling

NCX-labeled vesicular structures in 10d ($N = 70$ cells from four animals) and 20d cells ($N = 56$ cells from four animals) were manually counted under the microscope by focusing through the depth of each cell. The longitudinal periodicity of transverse rows of NCX or RyR labeling was determined using the measurement probe from Imaris 4.0 (Bitplane) software. Sample size for each measurement is shown with data.

Fitting peripheral RyR intercluster distance data

Results of peripheral RyR periodicity from each of the five age groups exhibited a bimodal distribution and was well described by the sum of two Gaussian functions (Origin 7 SR1 software, OriginLab, Northampton, MA),

$$Probability = \frac{A_1}{\sqrt{2\pi}\sigma_1} e^{-\frac{1}{2}\left(\frac{x-x_1}{\sigma_1}\right)^2} + \frac{A_2}{\sqrt{2\pi}\sigma_2} e^{-\frac{1}{2}\left(\frac{x-x_2}{\sigma_2}\right)^2},$$

where A_1 and A_2 are the amplitudes, σ_1 and σ_2 are the widths of the Gaussian functions, and x_1 and x_2 are the two most probable intercluster distances. Quality fits were achieved for all age groups, as indicated by values of the correlation coefficient, ranging from 0.86 to 0.98.

Statistical analysis

All data expressed in the form of percentages or proportions had undergone arcsine transformation before performing statistical analyses (24). Statistical significance of results was determined by Student's *t*-test for paired samples or one-way analysis of variance (SPSS 13.0 software; SPSS, Chicago, IL). Multiple comparisons were performed using the Gabriel or the Games-Howell test (SPSS). All values were expressed as mean ± SE, unless otherwise stated.

RESULTS

We measured the regional distribution and colocalization of NCX and RyR in developing ventricular myocytes. Confocal images of dual-labeled cells were acquired, deconvolved, and digitally analyzed. Because a cardiomyocyte is too long to be imaged in its full length under high magnification, we selected only the central cell region for both analysis and projection. All images are representative of each age group, although developmental variations existed within each group; some myocytes were either less or further developed than the majority within the same heart.

NCX immunolabeling

3d (neonate)

Fig. 1 *A* displays images of NCX distribution in a 3d myocyte dual-stained for both NCX and RyR (images of RyR labeling are shown in Fig. 3 *A*). The 3-D reconstruction of NCX label shows a relatively slender cell exhibiting an abundance of immunofluorescence (Fig. 1 *Aa*, *top*). Because newborn rabbit ventricles do not have T-tubules (25), cross-sectional images confirm that the observed staining is restricted to the surface membrane (Fig. 1 *Aa*, *bottom*). A magnified view of only the surface label illustrates NCX being organized in closely spaced, discrete clusters (Fig. 1 *Ab*).

Images acquired from the cell center revealed a punctate NCX distribution (Fig. 1 *Ac*). NCX clusters were arranged at periodical intervals along the cell edge; the inset provides a magnified view of this orderly spacing, observed in all 3d cells examined and occurred throughout much of the cell.

An identical series of experiments were performed on 6d myocytes; the data obtained were virtually identical to that of 3d. Therefore, the 6d data are only graphically presented and not described in the text hereinafter.

10d and 20d (adolescent)

Surface distribution of NCX in 10d and 20d cells appeared similar to the 3d distribution. At 10d, most NCX was still orderly distributed at the cell surface, but the majority of cells had a low to moderate level of labeling at the cell interior (Fig. 1, *Ba* and *Bb*). A notable feature of this interior staining is that there were two patterns. In one, NCX label projected as short extensions from the surface membrane into the cytoplasm (Fig. 1 *Ba*, *bottom*, *single arrow*). T-tubule formation in rabbit ventricles occurs postnatally at ~10 days of age (25), consistent with the pattern just described.

In the other pattern, NCX was distributed on the periphery, or the surface, of small vesicular-like structures, located near the outer zone of the cytoplasm (Fig. 1 *Bb*, *single arrow*). The majority of cells expressed these structures, ranging from ~5 to ~30 per cell. One of the structures within the cell was isolated and magnified (Fig. 1 *Bb*, *bottom*). Some structures had no obvious connection to the surface membrane and appeared suspended in the cytoplasm; Fig. 1 *Bc*, *top*, shows a side (*xz*) view of a structure (*single arrow*) having no visible link to the surface membrane (*double arrows*), although it is possible that the labeling of potential connections were too dim for our system to detect. Yet, other structures appeared connected to the surface sarcolemma; Fig. 1 *Bc*, *bottom*, illustrating a side view of another structure, shows an apparent link between the edge of the structure and the cytoplasmic end of a surface membrane invagination.

At 20d, NCX distribution appeared similar to that of 10d. Surface NCX clusters were closely spaced in some, but not all, regions (Fig. 2 *Ab*). Internal NCX label became more abundant and extended further into the cytoplasm (Fig. 2, *Aa* (*bottom*, *single arrow*) and *Ab* (*double arrows*)). As in 10d, myocytes from this group also expressed NCX-labeled vesicular-like structures at the outer zones of the cytoplasm (Fig. 2 *Ab*, *single arrow*).

56d (adult)

Images of adult myocytes display a clear shift in the pattern of NCX distribution; most staining was at the cell interior.

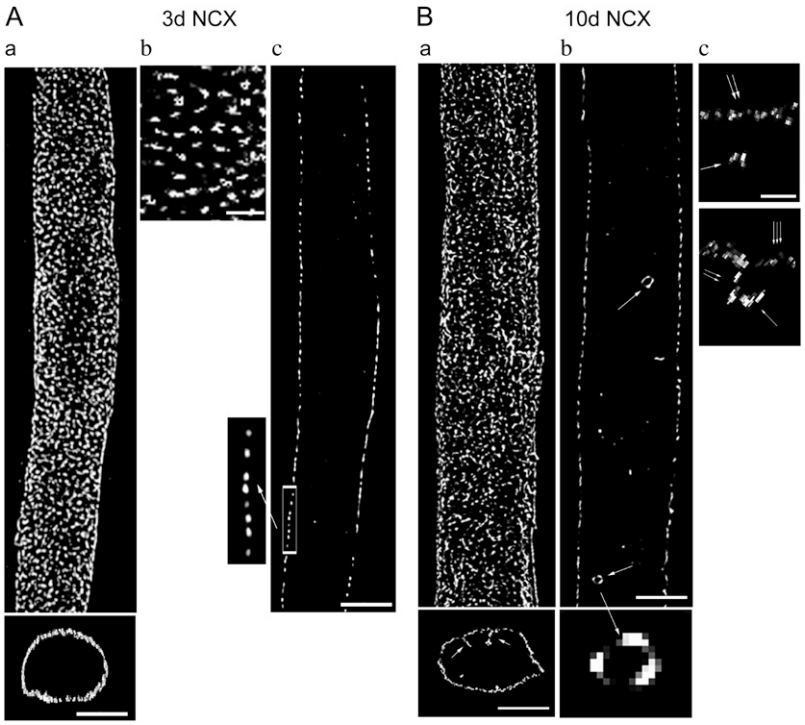

FIGURE 1 NCX distribution in 3d and 10d ventricular myocytes. (*A*) 3d. (*Aa*, *top*) 3-D reconstruction of NCX distribution; (*bottom*) a cross section of top image; section thickness = 5 μm; scale bar = 5 μm. (*Ab*) Magnified NCX label at cell surface, scale bar = 2 μm. (*Ac*) Single optical section, scale bar = 5 μm; (*inset*) magnified region of surface label. (*B*) 10d myocyte. (*Ba*, *top*) 3-D reconstruction of NCX distribution; (*bottom*) a cross section of top image; single arrows point to surface invagination; scale bar = 5 μm. (*Bb*, *top*) Single optical section (*single arrow* points to vesicular-like structures); (*bottom*) a magnified view of vesicular-like structure. (*Bc*, *top*) Magnified side view (*yz*) of a vesicular structure with no link to sarcolemma (*single arrow*, structure; *double arrow*, surface membrane; scale bar = 2 μm); (*bottom*) magnified side view (*yz*) of a structure with an apparent link to sarcolemmal invagination (*single arrow*, structure; *double arrow*, surface membrane invagination; *triple arrow*, surface membrane).

However, the regular periodicity of NCX distribution on the surface remained consistent with younger age groups. A magnified view of only the surface label (Fig. 2 *Bc*) from the 3-D reconstruction (Fig. 2 *Ba*) illustrates some clusters to be spaced further apart than those observed for 3d. Some surface labels were still closely distributed at some regions (Fig. 2 *Bb*, *single arrow*), but larger gaps emerged (*double arrows*). Interior clusters mainly organized in a series of transverse rows running perpendicular to the long axis of the cell. The longitudinal spacing of these rows concentrated at ~2.1 μm (N = 6 cells). Some label was also observed between the transverse rows (Fig. 2 *Bb*, *triple arrows*). A cell cross section reveals internal NCX labels forming tubular projections extending radially inward from the surface

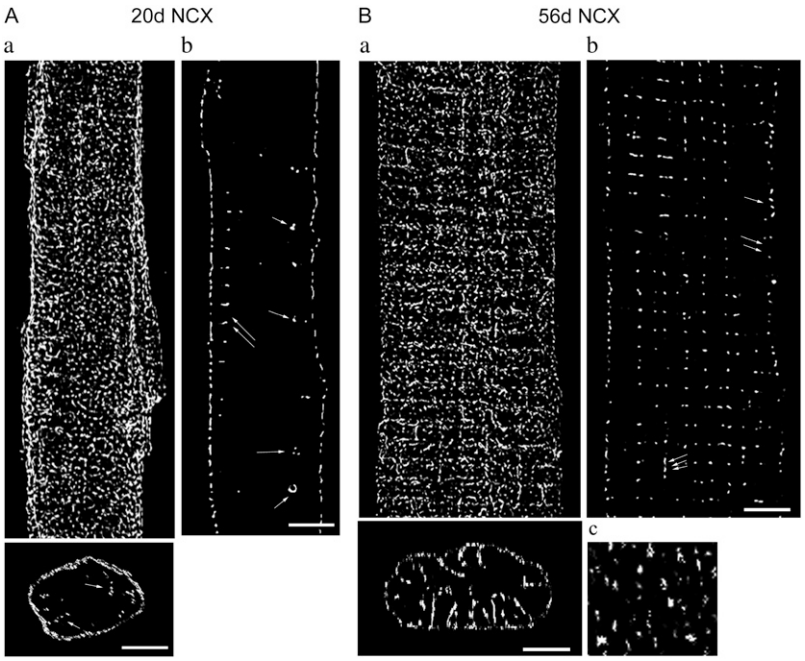

FIGURE 2 NCX distribution in 20d and 56d ventricular myocytes. (*A*) 20d myocyte. (*Aa*, *top*) 3-D reconstruction of NCX distribution; (*bottom*) a cross section of top image (*single arrow* points to surface membrane invaginations), scale bar = 5 μm. (*Ab*) Single optical section (*single arrow*, vesicular-like structures; *double arrows*, surface membrane invaginations; scale bar =5 μm). (*B*) 56d myocyte. (*Ba*, *top*) 3-D reconstruction of NCX distribution; (*bottom*) a cross section of top image, scale bar = 5 μm. (*Bb*) Single optical section at cell center (*single arrow*, closely spaced clusters; *double arrows*, widely spaced clusters; *triple arrows*, NCX label between the Z-lines, scale bar = 5 μm. (*Bc*) A magnified view of surface NCX label; scale bar = 2 μm.

membrane (Fig. 2 *Ba*, *bottom*). Of interest, there was a complete absence of NCX-labeled vesicular-like structures, seen in 10d and 20d, in these mature cells.

RyR immunolabeling

3d

Fig. 3 *A* displays images of the corresponding RyR staining for the 3d myocyte previously analyzed for NCX distribution. The 3-D reconstruction (Fig. 3 *Aa*, *top*) and its cross section (*bottom*) illustrate RyR labels being organized in discrete clusters, distributed in both the periphery (*bottom*, *single arrow*) and the interior (*double arrows*) of the cell. A magnified view of only the surface label is shown in Fig. 3 *Ab*. Images from the cell center revealed a highly organized RyR distribution along the cell edge (Fig. 3 *Ac*). The magnified region (*inset*) shows the receptor clusters closely spaced at periodic intervals, much like the 3d surface NCX.

At the interior, shown in Fig. 3 *Ac*, RyR distribution did not appear as highly organized as that seen at the periphery. In some places, RyR clusters distributed in a series of short transverse rows orientated perpendicularly to the cell's long axis (*single arrow*). The longitudinal distance of these rows was 1.97 $\pm$ 0.01 μm ($N = 10$ cells), which coincides with the sarcomeric spacing of myofibrils. At other regions, RyR clusters were less orderly spaced (*double arrows*). The black void (marked ''n'') at the cell center indicates an absence of antibody staining. In immature rabbit cardiomyocytes, myofibrils are generally confined to the cell periphery (26). A thin shell of myofibrils, only a few myofibrils deep, surrounds a central mass of nuclei and mitochondria, occupying a large fraction of the cell. This indicates that the void was not attributed to inaccessibility of anti-RyR, but represented the location of the cell nuclei and mitochondria.

10d and 20d

Unlike 3d, RyR clusters in the 10d (Fig. 3 *Ba*) and 20d (Fig. 4 *Aa*) cells localized mainly to the cell interior. Peripheral RyR staining became progressively sparse; some clusters were still narrowly spaced in some regions (10d, Fig. 3 *Bb*; 20d, Fig. 4 *Ab*, *single arrow*), but in other places, larger gaps emerged (*double arrows*).

Interior RyR clusters assumed a more orderly distribution than the 3d, arranged in a series of short transverse rows orientated perpendicularly to the cell's long axis (10d, Fig. 3 *Bb*; 20d, Fig. 4 *Ab*). The longitudinal periodicity of these rows were 2.02 $\pm$ 0.02 μm ($N = 8$ cells) for 10d and 2.04 $\pm$ 0.01 μm ($N = 8$ cells) for 20d.

56d

In mature myocytes (Fig. 4 *Ba*), the vast majority of RyR appeared to be in the interior; those located at the periphery had assumed a different distribution. Only a small fraction of

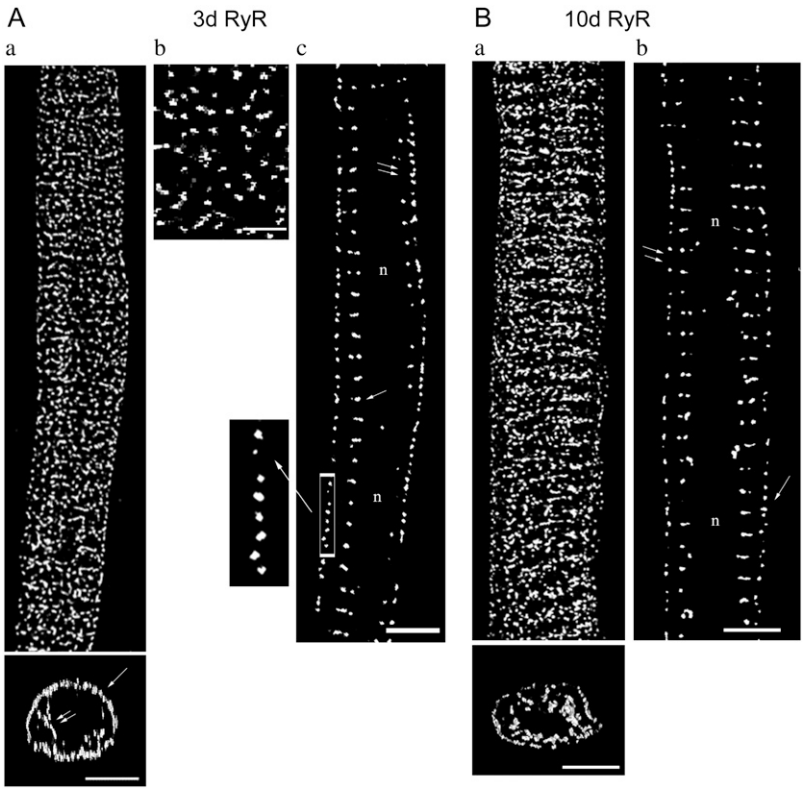

FIGURE 3 RyR distribution in 3d and 10d ventricular myocytes. (*A*) 3d myocyte. (*Aa*, *top*) 3-D reconstruction of RyR distribution; (*bottom*) a cross section of top image; single arrow, peripheral label; double arrows, internal label; scale bar = 5 μm. (*Ab*) Magnified RyR label at cell surface, scale bar = 2 μm. (*Ac*) Single optical section (*single arrow*, orderly spaced internal RyR; *double arrows*, sparsely spaced internal RyR; *n*, nuclear region); (*inset*) magnified view of surface label. (*B*) 10d myocyte. (*Ba*, *top*) 3-D reconstruction of RyR distribution; (*bottom*) a cross section of top image; scale bar = 5 μm. (*Bb*) Single optical section at cell center (*single arrow*, closely spaced peripheral RyR; *double arrows*, widely spaced peripheral RyR; *n*, nuclear region; scale bar = 5 μm).

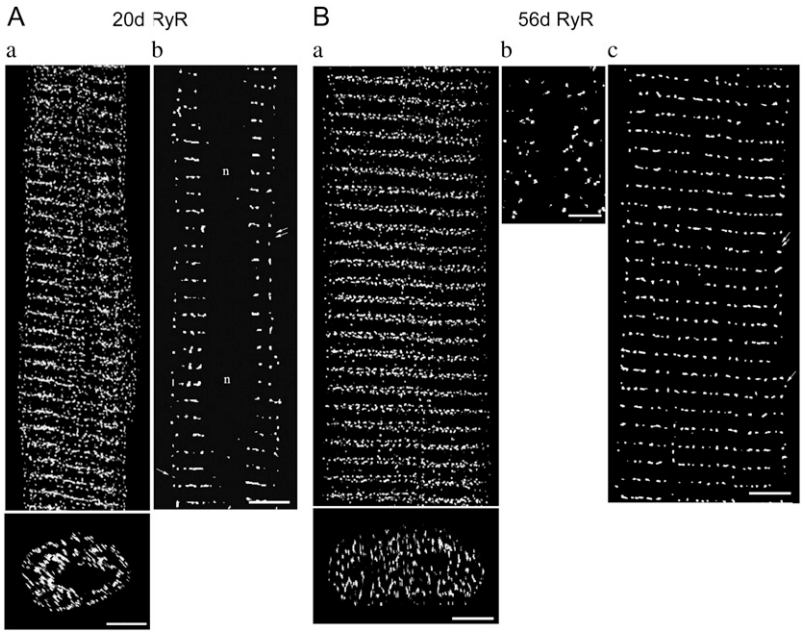

FIGURE 4 RyR distribution in 20d and 56d ventricular myocytes. (*A*) 20d myocyte. (*Aa*, *Top*) 3-D reconstruction of RyR distribution; (*bottom*) a cross section of top image; scale bar = 5 μm. (*Ab*) Single optical section (*single arrow*, label between the Z-line; *double arrows*, absence of label between Z-line; scale bar = 5 μm. (*B*) 56d myocyte. (*Ba*, *top*) 3-D reconstruction of RyR distribution; (*bottom*) a cross section of top image, scale bar = 5 μm. (*Bb*) Magnified RyR label at cell surface, scale bar = 2 μm. (*Bc*) Single optical section (*single arrow*, label between Z-line; *double arrows*, absence of label between Z-line; scale bar = 5 μm).

the peripheral clusters remained closely spaced (Fig. 4 *Bc*, *single arrow*); the majority of them exhibited relatively longer intercluster distances (*double arrows*). Interior RyR label became highly organized, distributed in a series of transverse rows periodically spaced at 2.04 ± 0.01 μm (N = 8 cells), in agreement with previous findings (18,19,27).

Measurements of NCX distribution

NCX fraction: surface versus interior

With development, the bulk of NCX label redistributed from the cell surface to the cell interior. To quantify this spatial transition, we mathematically divided each labeled cell into two cellular compartments—the surface and the interior. To achieve this, we digitally segmented each cell into cylindrical layers across its diameter, as shown in the NCX-labeled (*red*) 3d cell in Fig. 5 *A* (see ''Cell layering'' under Materials and Methods). The outermost layer of the surface label was layer 1; each successive inward layer was 1-voxel thick and numbered in ascending order. An additional layer was added just outside of layer 1 to account for the uncertainty in finding the surface.

A plot of the NCX fraction at each cell layer for all groups is shown in Fig. 6 *A*. In 3d cells, virtually all (94.2 ± 0.7%) of the NCX voxels resided within layers 1, 2, and 3. The lack of T-tubules in neonatal cells indicates these three layers collectively approximate the cell surface. Based on this, cells from all groups were additionally divided into two compartments, the surface (layers 1, 2, and 3) and the interior (remaining internal layers). The fraction of NCX located in each compartment is displayed in Fig. 6 *C*, showing that 3d cells expressed the highest surface proportion. With growth, the surface fraction declined steadily whereas the interior fraction gradually increased. The surface fractions for the 6d, 10d, 20d, and 56d were 92.5 ± 0.9%, 84 ± 1.0%, 77.0 ± 1.1%, and 32.8 ± 0.7%, respectively. In Fig. 6 *A*, the 56d curve shows a progressively drop in percent for the innermost cell layers. This drop reflects the progressive decrease in the layers' diameter while transitioning into the cell center.

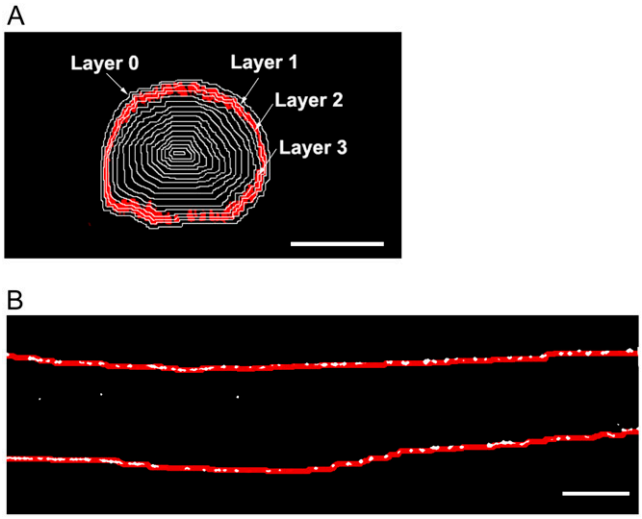

FIGURE 5 Cell layering and outline delineation. (*A*) Cross section of a 3d myocyte labeled for NCX (*red*) divided into layers (*white lines*; not drawn to scale) across the cell diameter; scale bar = 5 μm. (*B*) Single optical plane of a 3d ventricular myocyte stained for NCX (*white*). A 3-pixel-thick band (*red*; not drawn to scale) outlines the cell boundary.

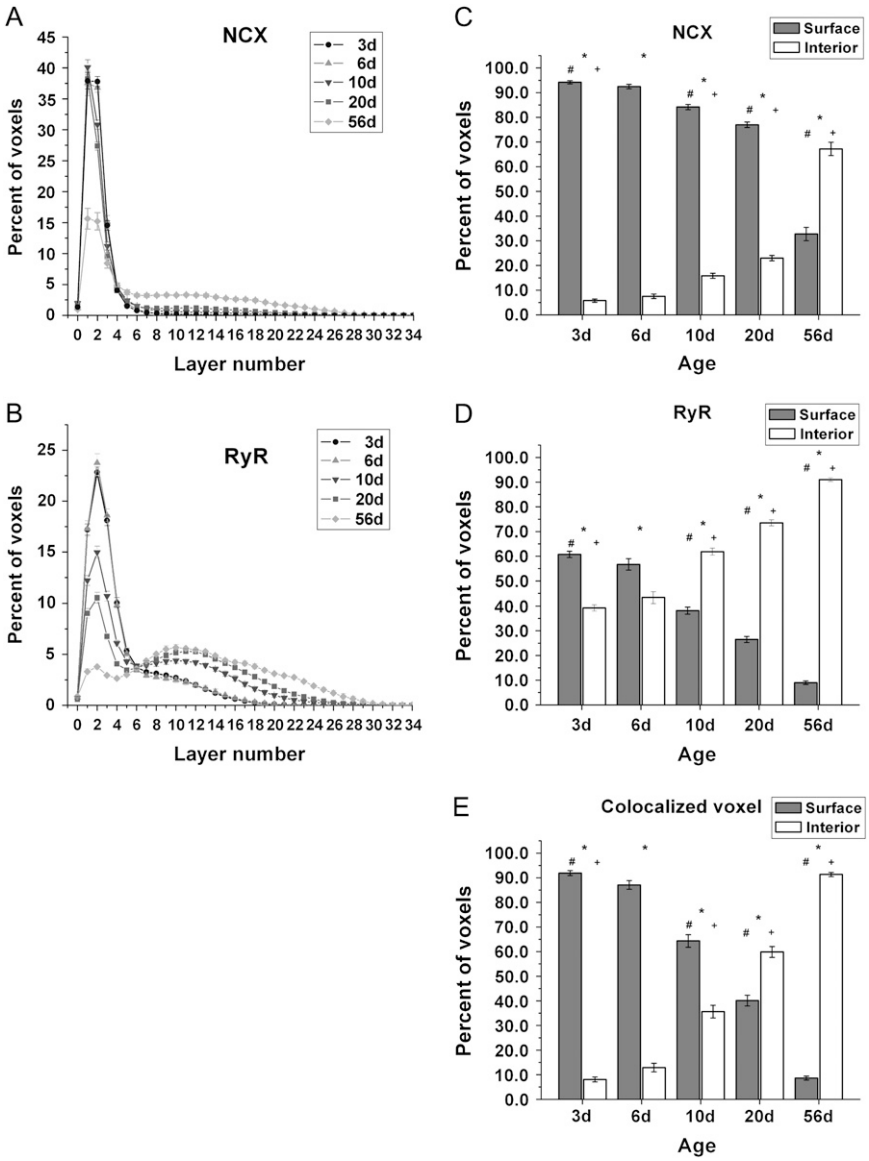

FIGURE 6 NCX or RyR fraction at different cell layers. (*A*) NCX fraction at different layers. (*B*) RyR fraction at different layers. (*C*) NCX, (*D*) RyR, or (*E*) colocalized voxel, fraction at surface (layers 1, 2, and 3) versus interior (remaining layers) compartment; * denotes a significant difference between surface and interior ($p < 0.05$); # denotes a significant difference in surface distribution between groups ($p < 0.05$), except for between 3d and 6d; + denotes a significant difference in interior distribution between groups ($p < 0.05$), except for between 3d and 6d.

Surface NCX intercluster distance

Our images show that NCX clusters at the cell surface were distributed in an orderly fashion in the neonate, but became increasing irregular with age. To mathematically capture this change, we measured the longitudinal distance between each pair of clusters along the cell boundary, which was delineated by a 3-pixel-thick band (*red*, Fig. 5 *B*; see Materials and Methods). Our calculation indicated at 3d, the most commonly observed intercluster spacing of surface NCX label occurred at ~0.7 μm (Fig. 7 *A*, *single arrow*). Further development to 6d, 10d, and 20d did not change the length of this dominant spacing. At maturity (56d), the intercluster distance was still most commonly registered at ~0.7 μm, but the probability of observing this spacing decreased significantly from younger groups ($p < 0.05$). Longer intervals were commonly seen; a second, smaller peak emerged at ~1.9 μm (Fig. 7 *A*, *double arrows*).

Measurements of RyR distribution

RyR fraction: surface versus interior

RyR distribution was prominent both in the cell periphery and the cell interior in the neonate, but by adulthood, most localized to the latter compartment. To quantify this age-dependent transition, the cell was divided into the same surface and interior volumes as previously described for the corresponding NCX label. Fig. 6, *B* and *D*, indicate the majority (60.7 ± 1.3%) of RyR at 3d was localized to the surface. We assume the peripheral receptors resided at the peripheral SR, but our optical system could not resolve the distance between the

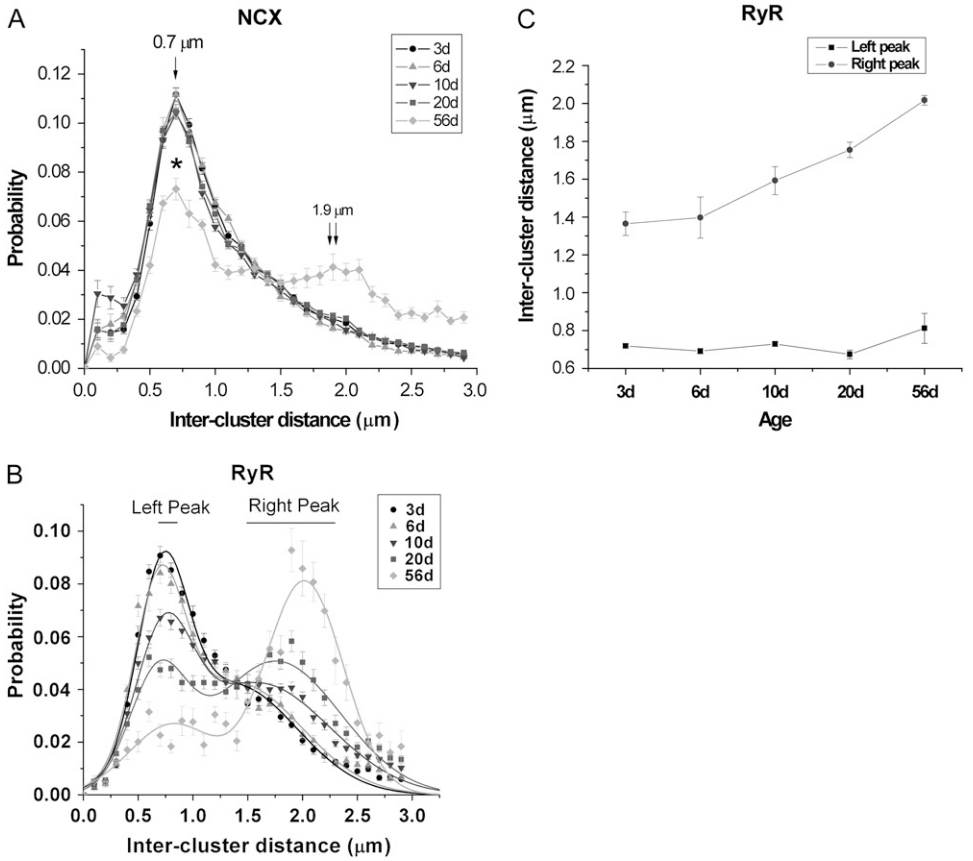

FIGURE 7 Intercluster distance of surface NCX or peripheral RyR. (*A*) Probability distribution of NCX intercluster distances; *y* axis denotes the probability of a particular intercluster spacing occurring within a cell; * denotes a significant difference between the 56d and the younger groups ($p < 0.05$). (*B*) Probability distribution of RyR intercluster distances well described by the sum of two Gaussian functions. The fits show each age group has two peak probabilities, denoted as left or right peak. (*C*) Peripheral RyR intercluster distance corresponded to the left or the right peak probability shown in panel *B*.

surface and the peripheral SR membranes; hence, receptors at the periphery were captured in the surface layers. Surface fractions for 6d, 10d, 20d, and 56d declined progressively with age; their values were 56.7 ± 2.3%, 38.2 ± 1.4%, 26.5 ± 1.2%, and 9.0 ± 1.8%, respectively. In Fig. 6 *B*, the progressive decline in percent for the innermost layers, shown in all groups, signifies a progressive decrease in the diameter of the inner layers.

Peripheral RyR intercluster distance

At 3d, RyR clusters near the cell surface were distributed at orderly, periodic intervals. With development, the interval between clusters appeared to lengthen. We measured the age-dependent change in peripheral RyR periodicity, applying the same method used for calculating the corresponding surface NCX intercluster distances.

Fig. 7 *B* shows the RyR periodicity data in all groups to exhibit a bimodal distribution, which was well described by the sum of two Gaussian functions (see Materials and Methods). The Gaussian fits indicate the most probable intercluster spacing for 3d cells occurred at 0.72 ± 0.01 μm (*left peak*; Fig. 7, *B* and *C*), almost identical to the corresponding NCX value. A second, smaller, peak probability occurred at 1.36 ± 0.07 μm (*right peak*, Fig. 7, *B* and *C*). With development, the left peak remained concentrated at from ~0.69 to ~0.81 μm, but the probability of recording these narrow spacings in a given cell dropped considerably with age. In contrast, the probability of observing the right peak increased with growth, along with a gradual increase in the length of spacing. By 20d, both the left (0.73 ± 0.12 μm) and right (1.75 ± 0.04 μm) peaks had almost equal probabilities. At adulthood, the left peak (0.81 ± 0.08 μm) diminished considerably whereas the right peak became dominant (2.02 ± 0.03 μm).

Colocalization

Whole cell and compartmental colocalization

In Fig. 8 (*top*) the merged 3-D reconstruction of NCX (*red*) and RyR (*green*) label in the 3d myocyte shows a considerable number of colocalized voxels (*white*) dispersed throughout the cell length. Colocalization analysis in the whole cell indicated 14.2 ± 0.7% of the voxels containing NCX also contained RyR (Fig. 9 *A*). Almost all of the colocalization (91.9 ± 1.0%; Fig. 6 *E*) occurred at the surface, further confirmed by a cell cross section (Fig. 8, *bottom*). We also measured colocalization in each cellular compartment; 13.0 ± 0.5% at the surface and only 1.0 ± 0.1% at the interior (Fig. 9 *A*).

At 10d and 20d (Fig. 9), colocalization in the whole cell declined significantly to 8.2 ± 0.4% and 8.0 ± 0.5%,

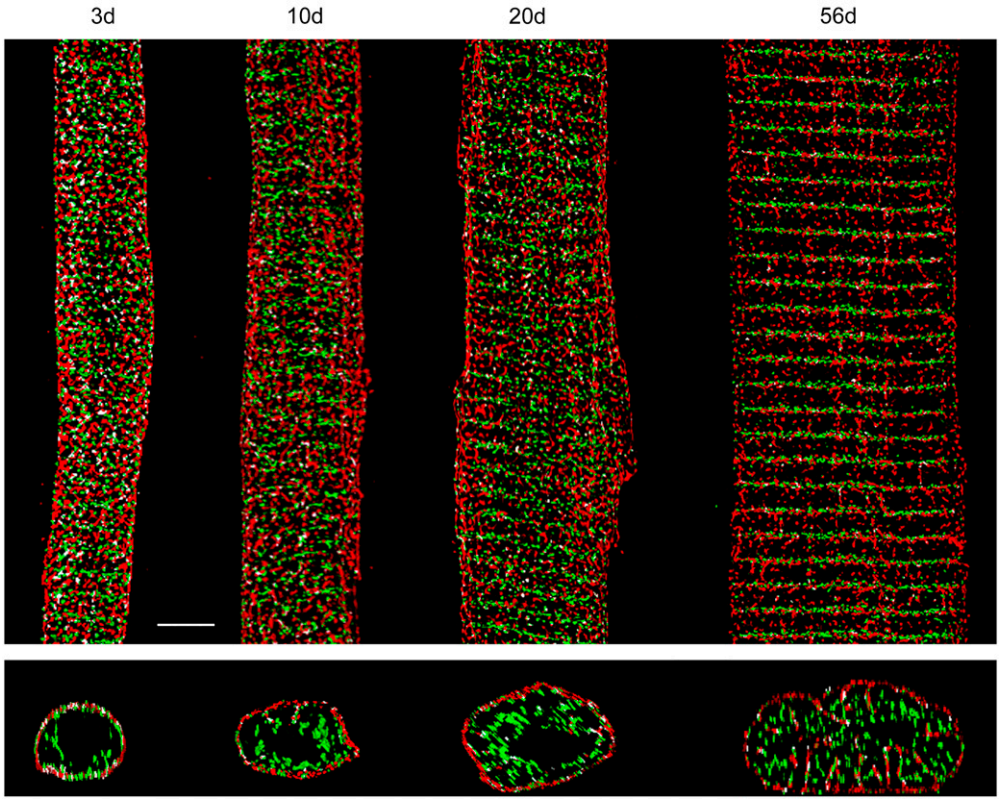

FIGURE 8 NCX and RyR colocalization in developing and matured ventricular myocytes. Merged images of NCX (*red*) and RyR (*green*) label previously shown; colocalized voxels are white; scale bar = 5 μm.

respectively. Colocalization was no longer restricted to the surface, but was also at the interior (Fig. 6 *E*). The compartmental breakdown of colocalization further confirmed this transition. At 56d, colocalization in the whole cell was 10.0 ± 0.6% (Fig. 9 *A*), significantly lower than that observed in 3d; the vast majority (91.4 ± 0.8%; Fig. 6 *E*) of colocalized voxels resided within the interior.

Colocalized voxel density

Although NCX and RyR colocalization in the whole cell decreased significantly from 3d to 56d, the percentage difference was small, giving an impression that their spatial relationship underwent little change with growth. Two crucial points that a colocalization percentage fails to convey in this study are the drastic developmental changes occurring in both cell size and NCX protein expression. The sarcolemmal area of neonatal rabbit ventricular myocytes is ~4.6-fold smaller than that of adults (28). Despite having a smaller surface, newborn NCX protein expression is ~2.5-fold greater than concentrations measured in adults (14). Given these age-dependent changes, having comparable colocalization percentages between newborns and adults does not necessarily translate into a similar distribution. Quite the contrary, the density of colocalized voxels (number of colocalized voxels per unit area cell compartment) in newborns appears to be substantially higher than that observed in adults, which could have important implications on cardiac E-C coupling.

To incorporate developmental changes (cell size and NCX expression level) into the colocalization equation, we normalized ''the number of colocalized voxels in a cell'' to ''the sarcolemmal volume of that cell'', which is the ''colocalized voxel density'' in a given cell. The reason we selected to normalize to the sarcolemma was because NCX distribution is largely restricted to the surface membrane and T-tubules of ventricular myocytes. However, we did not have measurements for the T-tubular volume because it was technically difficult to reliably stain for tubules, NCX, and RyR in the same cell. Thus, we normalized ''the number of colocalized voxels in a cell'' to only the surface compartment (in pL, delineated by layers 1, 2, and 3) of that cell. This method is the most appropriate for newborn myocytes exhibiting little or no T-tubules, but in 56d cells, T-tubules constitute ~42% of the total sarcolemmal area (29), indicating that this approach would grossly overestimate the colocalized voxel density in adults.

In Fig. 9 *B*, the 3d colocalized voxel density was 6403 ± 487 colocalized voxels per pL surface compartment, which is significantly higher than other groups. Values for 6d, 10d, 20d, and 56d (in colocalized voxels per pL surface compartment) were 6000 ± 585, 3504 ± 839, 2808 ± 996, and 2085 ± 215, respectively. Despite its overestimation, the adult measurement was only one-third of the neonatal value.

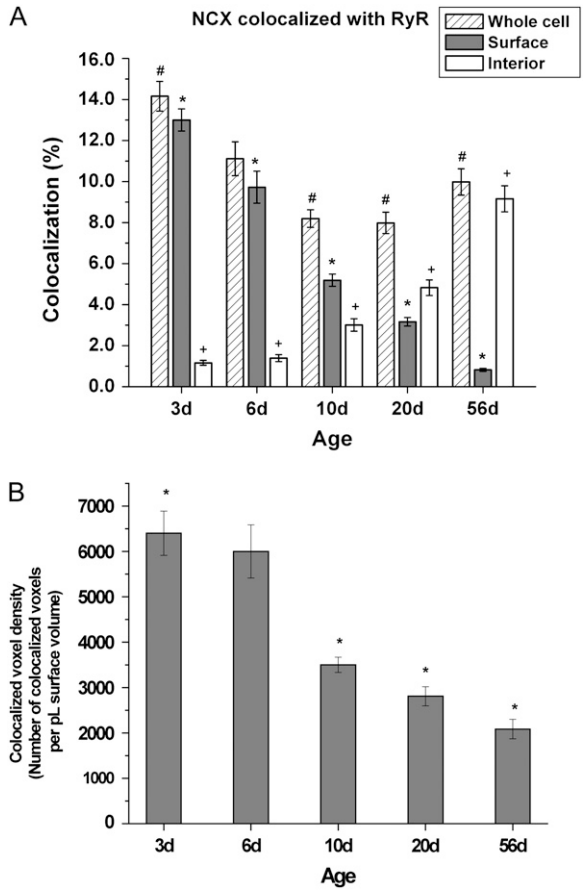

FIGURE 9 Whole cell NCX and RyR colocalization versus colocalized voxel density in developing and matured ventricular myocytes. (*A*) Colocalization in whole cell; # denotes a significant difference between 3d versus 10d, 20d, and 56d ($p < 0.05$); * denotes a significant difference between groups; + denotes a significant difference between groups ($p < 0.05$). (*B*) Colocalized voxel density (number of colocalized voxels per pL surface compartment); * denotes a significant difference between 3d versus 10d, 20d, and 56d ($p < 0.05$).

This large disparity was masked when colocalization was expressed in percentages.

DISCUSSION

We provide the first quantitative report of NCX and RyR distribution in developing ventricular myocytes using immunocytochemistry, confocal imaging, and digital image analysis. Programs used for image analyses in this study could potentially have widespread applications. The layering and intercluster distance analyses can be used in combination to quantify protein distribution at different cell regions in a variety of cell types. In addition, most of the analyses were automated to provide high throughput.

Our principal findings are: 1), NCX was largely localized to the surface sarcolemma in newborns; by adulthood, NCX also resided at the cell interior. 2), RyR was prominent both at the cell periphery and at the cell interior in neonates; at maturity, the receptors were concentrated mainly at the interior. 3), NCX and RyR distribution was highly organized in neonates and adults. 4), A relatively stable fraction (8–14%) of NCX colocalized with RyR in the whole cell during growth, but the colocalized voxel density in the adult was only one-third of the neonatal value.

NCX distribution

3d

The abundance of NCX label observed in the neonatal 3d cells is consistent with previous reports, which show that NCX expression is maximal near birth (13–15). This observation also highlights the exchanger's importance in delivering contractile Ca^{2+} to neonatal myofibrils. Virtually all of the fluorescent labeling was concentrated at the cell surface, demonstrating a lack of T-tubules in the newborns, as well as the specificity of the anti-NCX used in this study.

In addition, we uncovered a novel NCX distribution in these young cells; NCX clusters at the cell surface were spaced orderly at ~0.7 μm, about one-third the length of a relaxed sarcomere (26). This surprisingly organized pattern stands in sharp contrast with all past reports, which immunocytochemically show that NCX is apparently distributed homogeneously at the surfaces of neonatal rabbit ventricular myocytes (7,30). One of these studies (7) used the same anti-NCX employed in our work; indicating the differences likely did not arise from labeling with a different antibody clone. We ascribe this discrepancy to variations in cell isolation, fixation, and labeling procedures, all of which critically impact the staining pattern. The highly ordered and specific location of the exchanger may be of importance for understanding Ca^{2+} fluxes associated with E-C coupling in the neonate, as discussed further below.

The small fraction (~9%) of NCX voxels detected in the interior likely arose from two sources. First, the small amount of internal staining may signify NCX molecules undergoing posttranslational modifications at the SR and Golgi, subcellular trafficking or degradation. Second, there may be errors in identifying the cell surface layers due to the nature of the plasma membrane. The sarcolemma of a cardiomyocyte has uneven edges, steps, and folds (25), all of which decreases the accuracy in identifying the cell surface. A small fraction of the steps and folds of the cell surface may be included in the subsarcolemmal interior layers.

10d, 20d, and 56d

As development progresses to 10d and 20d, most NCX was still distributed at the cell surface, but the interior fraction increased significantly from the 3d value, coincident with the onset of T-tubule development. Of interest, NCX label was observed on the surface or the periphery of vesicular-like structures located at the outer zone of the cytoplasm. These

structures were present only in cells undergoing T-tubule biogenesis; they were completely absent in cells without T-tubules (3d) and in cells with fully developed T-tubules (56d). Further work is required to uncover the function of these vesicular-like structures in ventricular myocytes undergoing T-tubule development.

At 56d, the majority (67.2 ± 2.7%) of NCX was located at the cell interior. The internal staining pattern closely resembled the complex morphology of a mature T-tubule network containing both transverse and axial elements (31), and is in good agreement with past immunocytochemical findings (5,7,18,30,32,33). The primary function of NCX in adult ventricular myocytes is Ca^{2+} extrusion. The vast majority of Ca^{2+} entering the cell via DHPR during systole is removed by the exchanger (34). In adult rabbit ventricles, most of the dyadic junctions are concentrated in T-tubules, with relatively few dyadic sites at the surface membrane (29). Our measurements indicate that most NCX, responsible for Ca^{2+} extrusion, was likely localized to T-tubules where major calcium release sites reside, consistent with previous functional work (35).

RyR distribution

3d

The few studies examining RyR distribution in neonatal ventricular myocytes qualitatively show the receptors to locate mainly at the cell interior (7,19), where they arrange in an array of rows parallel to the level of the Z-line (19). We observed a similar interior RyR organization, based on the longitudinal spacing of short transverse rows of labeling, but additionally noted a highly organized distribution near the surface membrane. At the cell periphery where the majority (60.7 ± 1.3%) resided, RyR clusters were orderly spaced at narrow intervals of ~0.7 μm. This new finding implicates that there was a dense network of Ca^{2+} release sites at the subsarcolemma of newborn myocytes.

In both developing (36) and mature (37) ventricular myocytes, RyR molecules are largely clustered at specialized SR junctions, closely apposing either the surface membrane (forming peripheral couplings) or T-tubules (forming dyads). RyR clusters are also found in specialized SR domains that do not form junctions with the sarcolemma, known as corbular SR. These specialized junctions, including corbular SR, are functionally equivalent and are named Ca^{2+} release units (CRUs) (37). Ultrastructural studies show that peripheral couplings are the first to occur during cardiac development, followed by the formation of corbular SR. With the development of T-tubules, the dyads appear (36).

In this study, the narrowly spaced peripheral RyR clusters were likely located at the peripheral SR, where they juxtaposed the surface membrane to form peripheral couplings. In congruence with this view, our previous ultrastructural work demonstrated that the subsarcolemmal SR in 3d rabbit ventricular myocytes appear to form sheet-like structures extending along the apposing sarcolemma and were determined to be ~3 times longer than those in adult cells (38). The RyR fraction we observed at the interior maybe localized to the corbular SR, since T-tubules had not yet been formed.

10d, 20d, and 56d

With development to 10d and 20d, RyR distribution shifted progressively from the periphery to the interior. By adulthood, the vast majority (91.0 ± 0.7%) of RyR was at the interior, where they were mainly organized in transverse rows periodically spaced at ~2.0 μm, coinciding with the sarcomeric Z-line pattern of myofibrils. RyR molecules are known to locate largely in the SR membrane adjacent to the T-tubules of adult cardiac myocytes (27,37), indicating the receptor staining was likely localized to the dyadic junctions along the Z-lines.

At the cell periphery, the most probable RyR intercluster distance rose gradually from ~0.7 μm at 3d, to ~2.0 μm at 56d (Fig. 7, *B* and *C*). If the longitudinal spacing of interior clusters were used to infer the Z-line's position, then the peripheral labels, which once interspersed between Z-lines or at a peri-M-line position, of young cells were largely absent in adults. Because the predominant intercluster spacing in matured myocytes is comparable to the length of a relaxed sarcomere (26), some of the subsarcolemmal receptor clusters may be distributed near the mouth of T-tubules, which have been shown to have a similar longitudinal spacing of ~1.8 μm (31). A word of caution is required for the estimate of intercluster distances. Two-dimensional techniques are highly dependent on the corresponding alignment between the imaging plane of the microscope and the alignment of the cellular structure being investigated. This relationship, coupled with finite limitations in resolution, allows clusters above and below the analysis plane to interfere. Given the z axis resolution (~620 nm) of the confocal microscope, applying deconvolution to all our images before analyses could only minimize, but not completely eliminate, the out-of-focus fluorescence emitting from adjacent planes. This out-of-focus signal could lead to a systematic underestimation of the apparent intercluster distances for peripheral NCX or RyR (20).

A recent study shows intense peripheral RyR staining between the Z-lines of rat adult ventricular myocytes and indicates these labels are absent in overpermeabilized myocytes (20). We, on the other hand, commonly observed peripheral RyR label between the Z-lines of neonatal myocytes, but not in mature cells. Newborn cardiomyocytes are far more fragile than those of adults; yet we consistently generated clean, reproducible staining in this age group. Hence, the paucity of peripheral RyR label in the 56d myocytes we studied could not be ascribed to cell overpermeabilization. Ventricular contractions in rats have been shown to have a greater reliance on SR Ca^{2+} release than that observed in rabbits (39). Hence,

the discrepancy may be attributed, in part, to the use of a different animal species.

Peripheral versus interior subpopulation

Based on their regional distribution, we postulate that there are two subpopulations of RyR in rabbit ventricular myocytes: the interior and the periphery. The expression patterns of the two subgroups appear to be reciprocal with development. In neonatal cells, peripheral clusters were highly expressed and narrowly spaced; internal clusters, although abundant, are less organized. At maturity, the peripheral clusters became less closely spaced, assuming a similar intercluster distance as that of their interior counterparts, which were highly organized at the Z-lines. Consonant to this view, functional studies have shown that Ca^{2+} sparks, elementary events of SR Ca^{2+} release (40), occur primarily at the periphery of neonatal rabbit and rat ventricular myocytes (7,41). When these cells reached maturity, sparks were detected throughout the width of the cell, mainly along the Z lines at the cell interior (41). In adult rat ventricular myocytes, Ca^{2+} sparks at the cell interior has been shown to originate specifically from the T-tubules (42).

On a cautionary note, we cannot completely rule out the possibility that NCX or RyR distribution differences observed between groups may be attributed to differences in epitope accessibility. We did, however, devote extensive effort to optimizing our fixative and labeling protocols for epitope accessibility. We tested different concentrations of fixative, triton X-100, primary antibodies, and secondary antibodies, as well as different lengths of incubation period for each reagent concentration. In our selected protocol, the fixative and permeability agents were kept to a minimal to avoid excessive cross-linking and extraction of antigens, respectively. This approach produced labeling of the highest contrast and reproducibility and concomitantly optimized epitope accessibility.

Colocalization: a potential link to E-C coupling

We observed three distinguishing features in neonatal (3d) NCX and RyR distributions that make them likely candidates for functional coupling. First, both were highly expressed at or near the cell surface. Second, their distribution at or near the cell surface was highly organized with the identical predominant intercluster spacing. Third, their colocalized voxel density was maximal in 3d cells. Taken together, neonatal myocytes contain the largest number of potential coupling sites per pL cell surface, all of which concentrated in one compartment, the surface membrane.

Like the 3d cells studied, adult atrial myocytes of most mammalian species do not exhibit T-tubules (27,43), and have a network of Ca^{2+} stores both close to the sarcolemma and deep inside the cell (44). A depolarization-induced Ca^{2+} influx via sarcolemmal DHPR triggers Ca^{2+} release only from those RyR clusters located at the peripheral SR (43,45,46). Initially, discrete release sites at the periphery are activated; the signal spreads quickly to adjacent peripheral sites to form a subsarcolemmal ring of elevated cytosolic Ca^{2+}. This signal spreads inward and evokes a centripetally propagating Ca^{2+} wave, simultaneously eliciting peripheral and central myofibril contraction.

An analogous event could occur in neonatal ventricular myocytes, which express a high density of surface NCX and have a dense network of both peripheral and internal Ca^{2+} release sites. Previous work shows Ca^{2+} influx through reverse-mode NCX is sufficient to directly stimulate contraction in neonatal, but not adult, rabbit ventricular myocytes (12,13). This age-dependent difference was attributed to neonatal cells having a larger (approximately sixfold) NCX current density and a greater (approximately two- to threefold) surface area/volume ratio. On a similar note, our laboratory (28) and others (6) recently show that the neonatal rabbit SR has a larger (approximately threefold) Ca^{2+} store (normalized per unit cell volume) than that of adult, and that neonatal and adult cardiac RyR have similar gating and kinetic properties in planar lipid bilayers.

In addition, we recently demonstrated in neonatal rabbit ventricular myocytes that calcium influx via NCX could stimulate CICR, which accounted for ~40% of the Ca^{2+} transient; the process diminished with development (16). Imaging data presented in this study provide a potential structural basis for this functional finding. In the neonate, Ca^{2+} influx via reverse-mode NCX during systole could trigger Ca^{2+} release from the dense population of peripheral RyR clusters and generate an inward propagating Ca^{2+} wave. Although whole cell colocalization in 3d cells was only a moderate ~14%, the narrow spacing of both NCX and RyR at the cell surface and their relatively high colocalized voxel density may be important in attaining the CICR component. The colocalized sites could represent discrete sites of Ca^{2+} signal initiation, which rapidly spreads to adjacent peripheral Ca^{2+} release sites to create a subsarcolemmal ring of elevated Ca^{2+}.

In support of this view, a recent study of adult cardiac E-C coupling, using mathematical modeling, shows peripheral RyR clusters (or CRUs) located between the Z-lines to be responsible for increasing the likelihood of Ca^{2+} wave generation in adult atrial cardiomyocytes (47); the closer the CRUs, the higher the probability of wave initiation. This suggests that the narrow spacing (~0.7 μm) of RyR clusters at the neonatal cell periphery could be of importance in sufficiently elevating Ca^{2+} concentration at the subsarcolemma to initiate an inward propagating Ca^{2+} wave. We calculated the distance between the peripheral and the first interior rows of RyR clusters to be 1.06 ± 0.07 μm ($N = 10$ cells).

The remaining NCX population (~86%) that was not colocalized, or potentially coupled, with RyR in the neonate was likely responsible for only transporting Ca^{2+} into the cell during systole, without eliciting SR Ca^{2+} release. Influx

via uncoupled exchangers may mainly activate myofibrils that are located directly under the cell membrane, whereas the coupled exchangers could elicit CICR and initiate an inward propagating Ca^{2+} wave to activate interior myofibrils. In neonatal ventricular myocytes, myofibrils are mainly located at the cell periphery, which may explain why only a moderate fraction of NCX is needed to mediate CICR.

It is well established that DHPR-mediated CICR is the dominant mode of E-C coupling in the mature mammalian myocardium (1). In adult rabbit myocytes (56d), whole cell NCX and RyR colocalization was ~10% and their colocalized voxel density was 2085 voxels per pL surface compartment; the latter was only one-third of the neonatal value, suggesting that adult cells contained the lowest number of potential coupling sites. Our colocalization percentage was slightly higher than the value reported by Scriven et al. (18), although these authors performed their studies in adult rat. Despite these low values, there is electron microscopy data to show that in the adult rat ventricle, some NCX gold particles are in close proximity to RyR particles, at distances comparable to those measured between RyR and DHPR particles (48). The importance of NCX in initiating CICR in adult ventricular myocytes during systole is still debated. Some studies show the depolarization-induced Ca^{2+} influx via reverse-mode NCX could trigger SR Ca^{2+} release (49–56), whereas others measured little or no response (57–60).

SUMMARY AND CONCLUSIONS

In this study, we found NCX to be organized in a punctuate pattern at the cell surface throughout development. Our data also indicate the distribution of NCX and RyR to vary considerably with age. NCX located largely at the surface sarcolemma in newborns and redistributed to the cell interior at adulthood. RyR was prominent at both the cell periphery and the cell interior but concentrated at the interior upon maturity. Neonatal NCX or RyR clusters located at or near the surface sarcolemma were orderly spaced at narrow intervals; two-dimensional image analysis showed the longitudinal periodicity of these clusters to be concentrated at ~0.7 μm. Because of the previously described confounding factors, the peak periodicity value of ~0.7 μm may be underestimated. The spacing of surface NCX clusters did not vary appreciably with age, but the periodicity of peripheral RyR clusters underwent a significant change, occurring mainly at ~2.0 μm in adults. At maturity, interior NCX and RyR clusters were distributed primarily in transverse rows periodically spaced at ~2.0 μm. If the interior RyR labeling were consistent with the position of Z-lines in all groups, then the neonatal myocytes have a more prominent peri-M-line distribution in comparison to adults. Therefore, there may be a subpopulation of RyR that is prominent in the newborn heart and gradually decreases with development.

The colocalized voxel density in the neonate was approximately threefold greater than that observed in adults, suggesting the young cells expressed the highest number of potential coupling sites. Taken together, Ca^{2+} influx via NCX in the neonate could activate the dense network of peripheral SR Ca^{2+} stores via peripheral coupling, and evoke Ca^{2+}-induced Ca^{2+} release, eliciting the contraction of myofibrils located near the cell center. Ca^{2+} influx via the exchangers that were not colocalized with RyR may mainly activate subsarcolemmal myofibrils. In sum, NCX has multiple potential roles in neonatal E-C coupling: Ca^{2+} influx via the reverse mode to trigger CICR and to contribute to the Ca^{2+} transient; Ca^{2+} efflux via the forward mode to maintain low diastolic Ca^{2+} concentration.

SUPPLEMENTARY MATERIAL

To view all of the supplemental files associated with this article, visit www.biophysj.org.

We thank Drs. Ed Moore and David Scriven for their insightful discussions.

We are grateful for the generous support of the Canadian Institutes of Health Research and the Heart and Stroke Foundation of British Columbia and Yukon (to G.F.T.). J. Huang is the recipient of a Canada Research Scholarship from the Canadian Institutes of Health Research. G.F.T. is the recipient of a Tier I Canada Research Chair.

REFERENCES

1. Fabiato, A. 1983. Calcium-induced release of calcium from the cardiac sarcoplasmic reticulum. *Am. J. Physiol.* 245:C1–14.
2. Langer, G. A., and A. Peskoff. 1997. Role of the diadic cleft in myocardial contractile control. *Circulation.* 96:3761–3765.
3. Stern, M. D. 1992. Theory of excitation-contraction coupling in cardiac muscle. *Biophys. J.* 63:497–517.
4. Huang, J., L. Hove-Madsen, and G. F. Tibbits. 2005. Na^+/Ca^{2+} exchange activity in neonatal rabbit ventricular myocytes. *Am. J. Physiol. Cell Physiol.* 288:C195–C203.
5. Wetzel, G. T., F. Chen, and T. S. Klitzner. 1995. Na^+/Ca^{2+} exchange and cell contraction in isolated neonatal and adult rabbit cardiac myocytes. *Am. J. Physiol. Heart Circ. Physiol.* 268:H1723–H1733.
6. Perez, C. G., J. A. Copello, Y. Li, K. L. Karko, L. Gomez, J. Ramos-Franco, M. Fill, A. L. Escobar, and R. Mejia-Alvarez. 2005. Ryanodine receptor function in newborn rat heart. *Am. J. Physiol. Heart Circ. Physiol.* 288:H2527–H2540.
7. Haddock, P. S., W. A. Coetzee, E. Cho, L. Porter, H. Katoh, D. M. Bers, M. S. Jafri, and M. Artman. 1999. Subcellular $[Ca^{2+}]_i$ gradients during excitation-contraction coupling in newborn rabbit ventricular myocytes. *Circ. Res.* 85:415–427.
8. Klitzner, T. S., F. H. Chen, R. R. Raven, G. T. Wetzel, and W. F. Friedman. 1991. Calcium current and tension generation in immature mammalian myocardium: effects of diltiazem. *J. Mol. Cell. Cardiol.* 23:807–815.
9. Hohl, C. M., B. Livingston, J. Hensley, and R. A. Altschuld. 1997. Calcium handling by sarcoplasmic reticulum of neonatal swine cardiac myocytes. *Am. J. Physiol.* 273:H192–H199.
10. Tanaka, H., T. Sekine, K. Nishimaru, and K. Shigenobu. 1998. Role of sarcoplasmic reticulum in myocardial contraction of neonatal and adult mice. *Comp. Biochem. Physiol. A. Mol. Integr. Physiol.* 120:431–438.
11. Balaguru, D., P. S. Haddock, J. L. Puglisi, D. M. Bers, W. A. Coetzee, and M. Artman. 1997. Role of the sarcoplasmic reticulum in contraction and relaxation of immature rabbit ventricular myocytes. *J. Mol. Cell. Cardiol.* 29:2747–2757.

12. Haddock, P. S., W. A. Coetzee, and M. Artman. 1997. Na^+/Ca^{2+} exchange current and contractions measured under Cl^--free conditions in developing rabbit hearts. *Am. J. Physiol. Heart Circ. Physiol.* 273: H837–H846.

13. Artman, M., H. Ichikawa, M. Avkiran, and W. A. Coetzee. 1995. Na^+/Ca^{2+} exchange current density in cardiac myocytes from rabbits and guinea pigs during postnatal development. *Am. J. Physiol. Heart Circ. Physiol.* 268:H1714–H1722.

14. Artman, M. 1992. Sarcolemmal Na^+-Ca^{2+} exchange activity and exchanger immunoreactivity in developing rabbit hearts. *Am. J. Physiol.* 263:H1506–H1513.

15. Boerth, S. R., D. B. Zimmer, and M. Artman. 1994. Steady-state mRNA levels of the sarcolemmal Na^+-Ca^{2+} exchanger peak near birth in developing rabbit and rat hearts. *Circ. Res.* 74:354–359.

16. Huang, J., L. Hove-Madsen, and G. Tibbit. 2005. Ontogeny of Ca^{2+}-induced Ca^{2+} release (CICR) in rabbit ventricular myocytes. *Biophys. J.* 88:483a.

17. Frank, J. S., G. Mottino, D. Reid, R. S. Molday, and K. D. Philipson. 1992. Distribution of the Na^+-Ca^{2+} exchange protein in mammalian cardiac myocytes: an immunofluorescence and immunocolloidal gold-labeling study. *J. Cell Biol.* 117:337–345.

18. Scriven, D. R., P. Dan, and E. D. Moore. 2000. Distribution of proteins implicated in excitation-contraction coupling in rat ventricular myocytes. *Biophys. J.* 79:2682–2691.

19. Sedarat, F., L. Xu, E. D. Moore, and G. F. Tibbits. 2000. Colocalization of dihydropyridine and ryanodine receptors in neonate rabbit heart using confocal microscopy. *Am. J. Physiol. Heart Circ. Physiol.* 279:H202–H209.

20. Chen-Izu, Y., S. L. McCulle, C. W. Ward, C. Soeller, B. M. Allen, C. Rabang, M. B. Cannell, C. W. Balke, and L. T. Izu. 2006. Three-dimensional distribution of ryanodine receptor clusters in cardiac myocytes. *Biophys. J.* 91:1–13.

21. Sedarat, F., E. Lin, E. D. Moore, and G. F. Tibbits. 2004. Deconvolution of confocal images of dihydropyridine and ryanodine receptors in developing cardiomyocytes. *J. Appl. Physiol.* 97:1098–1103.

22. Maruoka, N. D., D. F. Steele, B. P. Au, P. Dan, X. Zhang, E. D. Moore, and D. Fedida. 2000. Alpha-actinin-2 couples to cardiac Kv1.5 channels, regulating current density and channel localization in HEK cells. *FEBS Lett.* 473:188–194.

23. Dan, P., J. C. Cheung, D. R. Scriven, and E. D. Moore. 2003. Epitope-dependent localization of estrogen receptor-alpha, but not -beta, in en face arterial endothelium. *Am. J. Physiol. Heart Circ. Physiol.* 284: H1295–H1306.

24. Anscombe, F. J. 1948. The transformation of poisson, binomial, and negative binomial data. *Biometrika.* 35:246–254.

25. Smolich, J. J. 1995. Ultrastructural and functional features of the developing mammalian heart: a brief overview. *Reprod. Fertil. Dev.* 7:451–461.

26. Nassar, R., M. C. Reedy, and P. A. Anderson. 1987. Developmental changes in the ultrastructure and sarcomere shortening of the isolated rabbit ventricular myocyte. *Circ. Res.* 61:465–483.

27. Carl, S. L., K. Felix, A. H. Caswell, N. R. Brandt, W. J. Ball Jr., P. L. Vaghy, G. Meissner, and D. G. Ferguson. 1995. Immunolocalization of sarcolemmal dihydropyridine receptor and sarcoplasmic reticular triadin and ryanodine receptor in rabbit ventricle and atrium. *J. Cell Biol.* 129:672–682.

28. Huang, J., L. Xu, M. Thomas, K. Whitaker, L. Hove-Madsen, and G. F. Tibbits. 2006. L-type Ca^{2+} channel function and expression in neonatal rabbit ventricular myocytes. *Am. J. Physiol. Heart Circ. Physiol.* 290:H2267–H2276.

29. Page, E., and M. Surdyk-Droske. 1979. Distribution, surface density, and membrane area of diadic junctional contacts between plasma membrane and terminal cisterns in mammalian ventricle. *Circ. Res.* 45:260–267.

30. Chen, F., G. Mottino, V. Y. Shin, and J. S. Frank. 1997. Subcellular distribution of ankyrin in developing rabbit heart–relationship to the Na^+-Ca^{2+} exchanger. *J. Mol. Cell. Cardiol.* 29:2621–2629.

31. Soeller, C., and M. B. Cannell. 1999. Examination of the transverse tubular system in living cardiac rat myocytes by 2-photon microscopy and digital image-processing techniques. *Circ. Res.* 84:266–275.

32. Kieval, R. S., R. J. Bloch, G. E. Lindenmayer, A. Ambesi, and W. J. Lederer. 1992. Immunofluorescence localization of the Na-Ca exchanger in heart cells. *Am. J. Physiol.* 263:C545–C550.

33. Scriven, D. R., A. Klimek, K. L. Lee, and E. D. Moore. 2002. The molecular architecture of calcium microdomains in rat cardiomyocytes. *Ann. N. Y. Acad. Sci.* 976:488–499.

34. Crespo, L. M., C. J. Grantham, and M. B. Cannell. 1990. Kinetics, stoichiometry and role of the Na-Ca exchange mechanism in isolated cardiac myocytes. *Nature.* 345:618–621.

35. Yang, Z., C. Pascarel, D. S. Steele, K. Komukai, F. Brette, and C. H. Orchard. 2002. Na^+-Ca^{2+} exchange activity is localized in the T-tubules of rat ventricular myocytes. *Circ. Res.* 91:315–322.

36. Franzini-Armstrong, C., F. Protasi, and P. Tijskens. 2005. The assembly of calcium release units in cardiac muscle. *Ann. N. Y. Acad. Sci.* 1047: 76–85.

37. Franzini-Armstrong, C., F. Protasi, and V. Ramesh. 1999. Shape, size, and distribution of Ca^{2+} release units and couplons in skeletal and cardiac muscles. *Biophys. J.* 77:1528–1539.

38. Huang, J., C. van Breemen, K. H. Kuo, L. Hove-Madsen, and G. F. Tibbits. 2006. Store-operated Ca^{2+} entry modulates sarcoplasmic reticulum Ca^{2+} loading in neonatal rabbit cardiac ventricular myocytes. *Am. J. Physiol. Cell Physiol.* 290:C1572–C1582.

39. Fabiato, A., and F. Fabiato. 1978. Calcium-induced release of calcium from the sarcoplasmic reticulum of skinned cells from adult human, dog, cat, rabbit, rat, and frog hearts and from fetal and new-born rat ventricles. *Ann. N. Y. Acad. Sci.* 307:491–522.

40. Cheng, H., W. J. Lederer, and M. B. Cannell. 1993. Calcium sparks: elementary events underlying excitation-contraction coupling in heart muscle. *Science.* 262:740–744.

41. Seki, S., M. Nagashima, Y. Yamada, M. Tsutsuura, T. Kobayashi, A. Namiki, and N. Tohse. 2003. Fetal and postnatal development of Ca^{2+} transients and Ca^{2+} sparks in rat cardiomyocytes. *Cardiovasc. Res.* 58: 535–548.

42. Shacklock, P. S., W. G. Wier, and C. W. Balke. 1995. Local Ca^{2+} transients (Ca^{2+} sparks) originate at transverse tubules in rat heart cells. *J. Physiol.* 487:601–608.

43. Kockskamper, J., K. A. Sheehan, D. J. Bare, S. L. Lipsius, G. A. Mignery, and L. A. Blatter. 2001. Activation and propagation of Ca^{2+} release during excitation-contraction coupling in atrial myocytes. *Biophys. J.* 81:2590–2605.

44. Michailova, A., F. DelPrincipe, M. Egger, and E. Niggli. 2002. Spatiotemporal features of Ca^{2+} buffering and diffusion in atrial cardiac myocytes with inhibited sarcoplasmic reticulum. *Biophys. J.* 83:3134–3151.

45. Bootman, M. D., D. R. Higazi, S. Coombes, and H. L. Roderick. 2006. Calcium signalling during excitation-contraction coupling in mammalian atrial myocytes. *J. Cell Sci.* 119:3915–3925.

46. Berlin, J. R. 1995. Spatiotemporal changes of Ca^{2+} during electrically evoked contractions in atrial and ventricular cells. *Am. J. Physiol.* 269: H1165–H1170.

47. Izu, L. T., S. A. Means, J. N. Shadid, Y. Chen-Izu, and C. W. Balke. 2006. Interplay of ryanodine receptor distribution and calcium dynamics. *Biophys. J.* 91:95–112.

48. Thomas, M. J., I. Sjaastad, K. Andersen, P. J. Helm, J. A. Wasserstrom, O. M. Sejersted, and O. P. Ottersen. 2003. Localization and function of the Na^+/Ca^{2+}-exchanger in normal and detubulated rat cardiomyocytes. *J. Mol. Cell. Cardiol.* 35:1325–1337.

49. Leblanc, N., and J. R. Hume. 1990. Sodium current-induced release of calcium from cardiac sarcoplasmic reticulum. *Science.* 248:372–376.

50. Litwin, S. E., J. Li, and J. H. Bridge. 1998. Na-Ca exchange and the trigger for sarcoplasmic reticulum Ca release: studies in adult rabbit ventricular myocytes. *Biophys. J.* 75:359–371.

51. Levi, A. J., P. Brooksby, and J. C. Hancox. 1993. A role for depolarisation induced calcium entry on the Na-Ca exchange in triggering intracellular calcium release and contraction in rat ventricular myocytes. *Cardiovasc. Res.* 27:1677–1690.

52. Nuss, H. B., and S. R. Houser. 1992. Sodium-calcium exchange-mediated contractions in feline ventricular myocytes. *Am. J. Physiol.* 263:H1161–H1169.

53. Kohomoto, O., A. J. Levi, and J. H. Bridge. 1994. Relation between reverse sodium-calcium exchange and sarcoplasmic reticulum calcium release in guinea pig ventricular cells. *Circ. Res.* 74:550–554.

54. Vornanen, M., N. Shepherd, and G. Isenberg. 1994. Tension-voltage relations of single myocytes reflect Ca release triggered by Na/Ca exchange at 35 degrees C but not 23 degrees C. *Am. J. Physiol.* 267: C623–C632.

55. Wasserstrom, J. A., and A. M. Vites. 1996. The role of Na^+-Ca^{2+} exchange in activation of excitation-contraction coupling in rat ventricular myocytes. *J. Physiol.* 493:529–542.

56. Lines, G. T., J. B. Sande, W. E. Louch, H. K. Mork, P. Grottum, and O. M. Sejersted. 2006. Contribution of the Na^+/Ca^{2+} exchanger to rapid Ca^{2+} release in cardiomyocytes. *Biophys. J.* 91:779–792.

57. Evans, A. M., and M. B. Cannell. 1997. The role of L-type Ca^{2+} current and Na^+ current-stimulated Na/Ca exchange in triggering SR calcium release in guinea-pig cardiac ventricular myocytes. *Cardiovasc. Res.* 35:294–302.

58. Sipido, K. R., M. Maes, and F. Van de Werf. 1997. Low efficiency of Ca^{2+} entry through the Na^+-Ca^{2+} exchanger as trigger for Ca^{2+} release from the sarcoplasmic reticulum. A comparison between L-type Ca^{2+} current and reverse-mode Na^+-Ca^{2+} exchange. *Circ. Res.* 81:1034–1044.

59. Bouchard, R. A., R. B. Clark, and W. R. Giles. 1993. Regulation of unloaded cell shortening by sarcolemmal sodium-calcium exchange in isolated rat ventricular myocytes. *J. Physiol.* 469:583–599.

60. Sham, J. S., L. Cleemann, and M. Morad. 1992. Gating of the cardiac Ca^{2+} release channel: the role of Na^+ current and Na^+-Ca^{2+} exchange. *Science.* 255:850–853.